

EFFICIENT TOPOLOGY OPTIMIZED COUPLERS FOR ON-CHIP SINGLE-PHOTON SOURCES: SUPPORTING INFORMATION

Omer Yesilyurt^{1,2,#}, Zhaxylyk A. Kudyshev^{1,2,#}, Alexandra Boltasseva^{1,2},
Vladimir M. Shalaev^{1,2}, and Alexander V. Kildishev^{1,*}

¹School of Electrical and Computer Engineering, Birck Nanotechnology Center and Purdue Quantum
Science and Engineering Institute, Purdue University, West Lafayette, IN 47906, USA

²Quantum Science Center, Oak Ridge, TN 37931, USA

[#]Authors with equal contributions

E-mail: kildisha@purdue.edu

Contents

S1 Setup for the Forward and Adjoint Simulations	S-3
S2 Setup for the Forward and Adjoint Simulations	S-3
S3 Setup for the Forward and Adjoint Simulations	S-6
S4 Setup for the Forward and Adjoint Simulations	S-8
References	S-9

S1 Setup for the Forward and Adjoint Simulations

Direct solver for full-wave numerical simulations in this study employs the finite-difference time-domain (FDTD) approximation (a commercial software suite, Lumerical FDTD is used). Configuration layouts for forward and adjoint simulations are shown in Figure S1. Both configurations use monochromatic sources with an excitation wavelength of 638 nm, matching the hBN zero-phonon emission line.

The forward simulation uses a dipole source to emulate the single-photon emitter. The lateral area of the coupler optimization domain is $2 \times 2 \mu\text{m}^2$ with a height of 200 nm. The coupler domain is connected to a waveguide with a matching height of 200 nm and a width of 500 nm. E - and H -fields at the waveguide are recorded with the monitor placed across the waveguide. At the adjoint simulation run, the dipole source is removed, and a perfectly matched waveguide mode source is placed at the monitor location from the forward simulation. The source excites only the fundamental mode of the waveguide. The amplitude of the mode excited by the source is determined from the coupling to the fundamental mode in the forward simulation. E - and H -fields in the coupler domain are recorded in both simulations and passed to the optimization engine for further calculations. The substrate and core materials are SiO_2 and Si_3N_4 . Refractive index values are taken as 1.48, 2.1, 2 for SiO_2 , Si_3N_4 , and hBN, respectively.

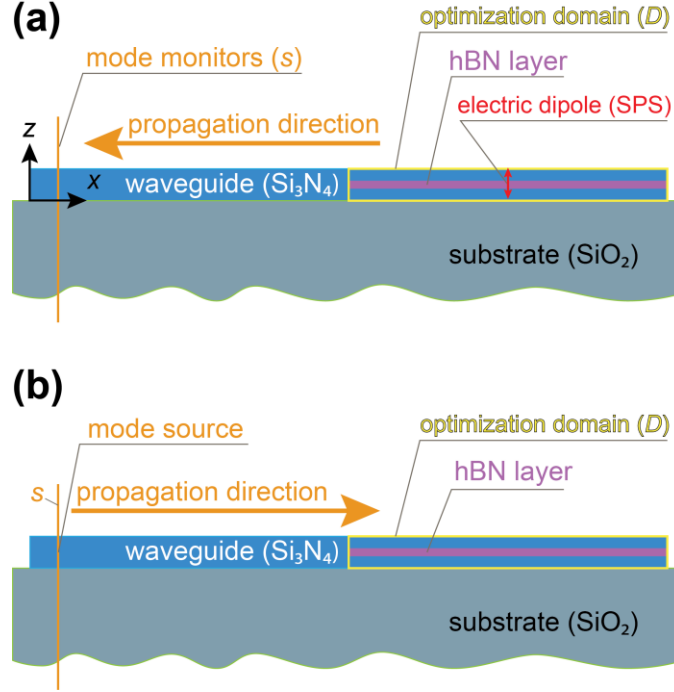


Fig. S 1. Configuration layouts for forward and adjoint simulations. (a) Forward simulation layout. The source for the forward simulation is an electric dipole (vertical red line with arrowheads), radiating energy into optimization domain D (purple box). E - and H -fields coupled to the waveguide are recorded by the mode monitors placed across the waveguide (orange line). Power coupling to the desired mode is also calculated at the mode monitor. Forward fields used for the optimization are also recorded in the optimization domain. (b) Adjoint simulation layout. The source for the adjoint simulation is a waveguide mode with the amplitude retrieved from forward simulation. Field propagation is reversed with respect to the forward simulation setup. Adjoint E -fields for optimization are recorded in D .

S2 Adjoint-Based Optimization for Single-Photon Emitter Couplers

Adjoint topology optimization is a powerful design technique leveraging the inherent symmetry in a general Maxwell operator for a reciprocal electromagnetic system.¹ This section presents the mathematical framework for the adjoint topology optimization used in our inverse design procedure for a high-efficiency single-photon emitter coupler. More general derivation for the adjoint method is available in the literature.^{2,3} The adjoint method uses only two simulations (forward and adjoint) per optimization iteration to calculate gradients of the dielectric function across the desired optimization area. The main goal of the optimization is to maximize the coupling efficiency between the single-photon emission energy with the fundamental mode of the waveguide. Hence, the coupling efficiency is employed as the optimization figure of merit (FoM).

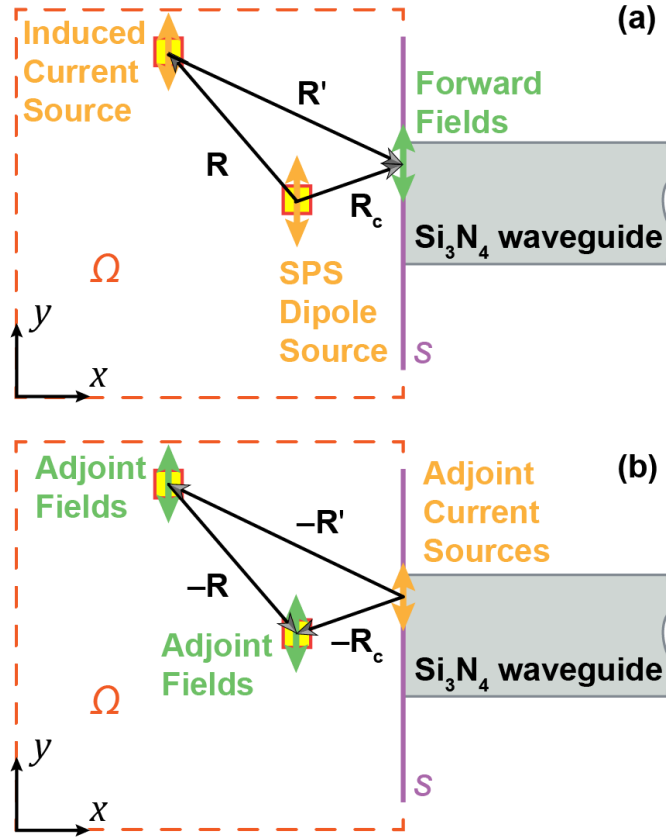


Fig. S 2. The forward (a) and adjoint (b) simulations schematic: these two steps are sufficient at each iteration. (a) The forward step: a single photon source (shown in orange) is excited inside the coupler. The induced dipoles are also shown in orange. The forward fields are obtained at cross-section Ω . FoM is calculated at the waveguide cross-section s . (b) The adjoint step: the adjoint source is excited at the waveguide cross-section s . The induced adjoint fields are shown in green.

Material density matrix. Reactive etching fabrication method adopted for the device restricts its geometry to multilayer shapes with translational symmetry in the vertical z -direction. Hence, we employ a density-based material parametrization following the onset discussed in^{4,5}, and utilize a 2D matrix of normalized (variation-limited) design parameters,

$$\rho = \begin{bmatrix} \rho_{11} & \cdots & \rho_{i_{\max}1} \\ \vdots & \ddots & \vdots \\ \rho_{1j_{\max}} & \cdots & \rho_{i_{\max}j_{\max}} \end{bmatrix} \quad (\text{S1})$$

Matrix ρ is used to map the normalized distribution over cross-section Ω , shown by the orange dashed box in Fig. 1(a) into the discretized permittivity distribution inside the entire coupler. Each term $\rho_{ij} = \rho(\mathbf{r}_{ij})$ of the material density matrix has a limited variation from 0 (air) to 1 (material), with $\mathbf{r} \in \Omega$ being a 2D position vector in Ω .^{42,4-7}

Coupling Efficiency (FoM). The normalized coupling efficiency is defined as the ratio of the squared electromagnetic energy flux converted into the lowest-order power-normalized TEM mode to the Poynting flux passing through the surface of a small cubic volume encapsulating the SPS,

$$C = \frac{|P|^2}{P_{\text{SPS}} P_0} \quad (\text{S2})$$

where

$$P = \frac{1}{4} \int_s (\mathbf{E} \times \mathbf{H}_0^* + \mathbf{E}_0^* \times \mathbf{H}) \cdot \hat{\mathbf{z}} ds \quad (\text{S3})$$

and

$$P_{\text{SPS}} = \frac{1}{2} \oint_{S_0} \Re(\mathbf{E}_d \times \mathbf{H}_d^*) \cdot d\mathbf{S}_0 \quad (\text{S4})$$

P and P_{SPS} are the power converted into the fundamental waveguide mode and power injected by the SPS into the simulation domain, respectively. \mathbf{E}_d and \mathbf{H}_d^* are the fields emitted by the dipole into the simulation domain, calculated at the surface of a small cubic shell (S_0) encapsulating the dipole. \mathbf{E}, \mathbf{H} fields generated by the SPS, and $\mathbf{E}_0, \mathbf{H}_0$ are the fields of the fundamental TEM mode pattern at the monitor cross-section area s . The overall objective of the TO cycle is obtaining the material density distribution (2D matrix ρ) in Ω , mapped into the permittivity distribution in optimization domain D , maximizing the coupling efficiency,

$$\max_{\rho} C(\mathbf{E}) \quad (\text{S5})$$

Filtering out the fundamental mode. We separate the power converted into the fundamental waveguide mode by presenting the fields (\mathbf{E}, \mathbf{H}) calculated at each iteration step, as a combination of the scaled fields of the fundamental mode ($a\mathbf{E}_f, a\mathbf{H}_f$), with a being a scaling factor, and some other modes $\mathbf{E} = a\mathbf{E}_0 + \mathbf{E}_\Sigma$ and $\mathbf{H} = a\mathbf{H}_0 + \mathbf{H}_\Sigma$,

$$\begin{aligned} P &= \frac{1}{4} \int_s (\mathbf{E} \times \mathbf{H}_0^* + \mathbf{E}_0^* \times \mathbf{H}) \cdot \hat{\mathbf{x}} ds \\ &= a \frac{1}{2} \int_s \Re(\mathbf{E}_0 \times \mathbf{H}_0^*) \cdot \hat{\mathbf{x}} ds + \underbrace{\frac{1}{4} \int_s (\mathbf{E}_\Sigma \times \mathbf{H}_0^* + \mathbf{E}_0^* \times \mathbf{H}_\Sigma) \cdot \hat{\mathbf{x}} ds}_{\text{orthonormality}} \end{aligned} \quad (\text{S6})$$

The second integral in (S6) vanishes due to the classical orthonormality condition between the fundamental and other waveguide modes.⁸ Hence, the initial integration of the calculated fields with (\mathbf{E}, \mathbf{H}) the normalized fundamental mode patterns ($\mathbf{E}_f, \mathbf{H}_f$) leaves only the power of the fundamental mode, where the fundamental mode patterns are normalized to give,

$$P_0 = \frac{1}{2} \int_s \Re(\mathbf{E}_0 \times \mathbf{H}_0^*) \cdot \hat{\mathbf{x}} ds = 1 [\text{W}]. \quad (\text{S7})$$

Induced field. It is assumed that a small perturbation of permittivity $\delta\epsilon_{ijk}$ excited with a local E -field generates a perturbation of the associated current density ($\delta\mathbf{J}_{ijk}$). For simplicity, the current density perturbation is taken directly proportional to the perturbation of voxel permittivity $\delta\epsilon_{ijk}$,

$$\delta\mathbf{J}_{ijk} = -i\omega\epsilon_0 [\delta\epsilon_{ijk} \mathbf{E}_{ijk}] \quad (\text{S8})$$

Then, a linear operator \mathbf{G}_{ijk} can be used, connecting the perturbation of inducing source⁹ $\delta\mathbf{J}_{ijk}$ with the perturbed induced field data $\delta_{ijk}\mathbf{E}$,

$$\begin{aligned} \delta_{ijk}\mathbf{E} &= \mathbf{G}_{ijk} \delta\mathbf{J}_{ijk}, \\ \mathbf{R}' &= \mathbf{R}_c - \mathbf{R}_{ijk} \end{aligned} \quad (\text{S9})$$

here \mathbf{G}_{ijk} is a general linear operator connecting the induced E -fields with inducing sources \mathbf{J}_{ijk} , respectively. The form of operator \mathbf{G}_{ijk} may vary depending on the actual solver used for calculating the field and could take different forms for the FEM^{3,4}, FDFD¹⁰, and other numerical techniques¹¹.

Efficiency gradient. As its name implies, a gradient-based optimization (S5), is built on computing the gradient of C . First, we connect the normalized field patterns $\omega\mu_0\mathbf{H}_0^* = \beta\hat{\mathbf{x}} \times \mathbf{E}_0^*$ (where $\beta = k_0k_z$ is a propagation constant). Then, we assume that a small perturbation of permittivity ($\delta\epsilon_{ijk}$) produces a small change to the E -field ($\delta_{ijk}\mathbf{E}$) at the waveguide cross-section S_c , $\mathbf{E} = a\mathbf{E}_0 + \delta_{ijk}\mathbf{E}$, and after neglecting the quadratic term, we get,

$$\delta_{ijk}C \approx \frac{2\Re\left(\int_s \delta_{ijk}\mathbf{E} \cdot A\mathbf{E}_0^* ds\right)}{P_{\text{SPS}}}, \quad A = a\eta_0k_z \quad (\text{S10})$$

with $\eta_0 = \sqrt{\epsilon_0/\mu_0}$.

The forward step: the scaling factor. Filtering procedure (S6) returns scaling coefficient $a = P/P_0$ at each forward step of the optimization cycle. Substituting (S9) into (S6) gives a perturbation of power generated by a perturbed voxel (with induced

current density \mathbf{J}_{ijk}) at the monitor cross-section s . Since for any $\mathbf{G} = (\mathbf{g}_x \ \mathbf{g}_y \ \mathbf{g}_z)^T$, $\mathbf{G} \in \mathbb{R}^{3 \times 3}$, $\{\mathbf{v}, \mathbf{w}, \mathbf{g}_i\} \in \mathbb{R}^3$, $i = \{x, y, z\}$, the following simplifying identity holds, $[\mathbf{G} \otimes \mathbf{v}] \cdot \mathbf{w} = \mathbf{v} \cdot [\mathbf{G}^T \otimes \mathbf{w}]$. Then,

$$\frac{\delta_{ijk} C}{\delta \varepsilon_{ijk}} \approx \frac{-2\Re(\mathbf{E}_{ijk} \cdot \mathbf{E}_{ijk}^{adjoint})}{P_{SPS}}, \quad \mathbf{E}_{ijk}^{adjoint} = \int_s (\mathbf{G}_{ijk}^T \otimes A\mathbf{J}_0^*) ds, \quad (\text{S11})$$

where $\mathbf{J}_0^* = i\omega\varepsilon_0\mathbf{E}_0^*$ is the adjoint current density generated by the adjoint E -field strength by the fundamental waveguide mode with a scaled field pattern \mathbf{E}_0^* . The integral in (S11) uses reciprocity to compute the adjoint field at the perturbed location ($\mathbf{E}_{ijk}^{adjoint}$).

The actual way of reconstructing the adjoint field in the device domain D from the field pattern depends on the selected solver.¹² In our case, a commercial FDTD solver has been used to obtain all the forward and adjoint fields. Equation (S11) gives the partial derivatives of C with a clear path to adjoint topology optimization (see, Section S3, page 6).

Purcell Factor. Since the overall emission is largely modified by the dielectric composition around the emitter, the Purcell factor is also affected by the optimization process. Purcell factor here is defined as the ratio of light flux going through a small cubic volume around the source between the optimized and the homogenous material distributions.

$$F_p = \frac{P_c}{P_h} = \frac{\frac{1}{2} \oint_{s_0} \Re(\mathbf{E}_d \times \mathbf{H}_d^*) \cdot d\mathbf{s}_0}{\frac{1}{2} \oint_{s_0} \Re(\mathbf{E}_d \times \mathbf{H}_d^*) \cdot d\mathbf{s}_0} \quad (\text{S12})$$

P_h and P_c are the time-averaged energy density fluxes going through a small box encapsulating the source inside optimization domain D , filled with either homogenous Si_3N_4 (P_h) or optimized binary Si_3N_4 -Vacuum composite (P_c).

S3 Iterative Optimization Procedure

The adjoint topology optimization is an iterative inverse design process typically lasting several hundred iterations for a design to converge. The number of iterations is strictly controlled by the gradient scaler (α), binarization push coefficient, filter radius, and initial condition. One can gain intuition into the proper selection of these parameters after a few initial runs. The optimization process is summarized in Fig. S 3. In the rest of this section, we follow the flowchart and lay out the details of each step.

Selecting the Initial Material Density Distribution. Initial material distribution is one of the most impactful factors in topology optimization since the gradient descent nature of the procedure finds the local minima which is dictated by the starting point in the optimization hyperplane.¹³ The initial distribution can either be set randomly or based on intuitive topologies for the specific design. In addition, the intuition behind the high-performance topologies can be deduced by inspecting the material distribution of the high-efficiency devices, which in return can inspire initial material distribution yielding even better performance characteristics. For the first part of this study, we randomly sampled the optimization plane for initial material density distribution. Later, we used intuitive starting points based on the high-performance topologies. Details of this procedure is discussed in Section S4.

Filtering and Binary Push. During the topology optimization, the dielectric constant at all spatial voxels in the device can range in continuous fashion between selected material platforms. The continuous distribution of the refractive index is realized by the material density matrix. The optimization procedure modifies the density matrix, which is later used to calculate the exact permittivity at each discrete voxel.

$$\begin{aligned} \varepsilon_{\text{air}} &< \varepsilon_{ij} < \varepsilon_{\text{mat}} \\ 0 &< \rho_{ij} < 1 \\ \varepsilon_{ij} &= \rho_{ij}\varepsilon_{\text{mat}} + (1 - \rho_{ij})\varepsilon_{\text{air}} \end{aligned} \quad (\text{S13})$$

where ρ_{ij} is the material density distribution that varies from 0 (air) to 1 (material); $\varepsilon_{\text{air}} = 1$ and ε_{mat} are the dielectric constants of air and the material domain (Si_3N_4 and hBN), respectively, $\varepsilon_{\text{mat}} \in \{\varepsilon_{\text{Si}_3\text{N}_4} = 2.1^2, \varepsilon_{\text{hBN}} = 4\}$.

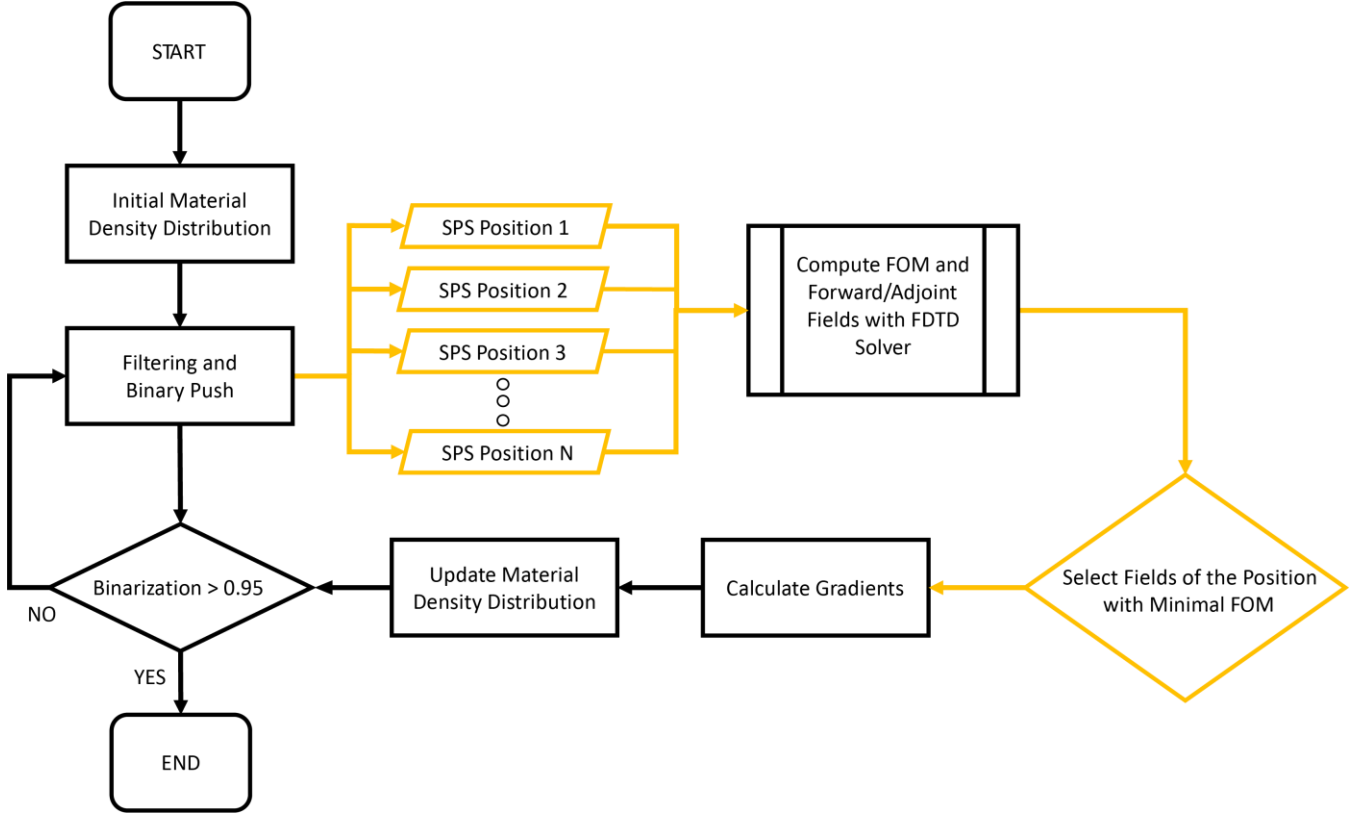


Fig. S 3. Flowchart of the optimization procedure.

Feature sizes in any photonic device are constrained by fabrication capabilities. To conform with state-of-the-art fabrication methods such as electron beam lithography, features with dimensions below a certain threshold need to be removed. These features include tiny protrusions from the central bodies of small islands of material/hole. To this end, we applied a circular spatial blurring filter to the material distribution every few tens of iterations,

$$\rho_e = \frac{\sum_{ij \in \mathbb{N}_e^{2 \times 2}} \rho_{ij} \left[r_{filter} - \frac{\|\mathbf{r}_{ij} - \mathbf{r}_e\|}{r_{filter}} \right]}{\sum_{ij \in \mathbb{N}_e^{2 \times 2}} \left[r_{filter} - \frac{\|\mathbf{r}_{ij} - \mathbf{r}_e\|}{r_{filter}} \right]} \quad (\text{S14})$$

where r_{filter} is the filter radius, $\mathbb{N}_e^{2 \times 2}$ is the set containing the grid points within the filter radius with respect to a given filtered point ρ_e . The filter radius is selected to be 60 nm for this study. The application of the filter reduces the FoM immediately since the optimized density matrix is blurred. However, this procedure is applied multiple times until a converged design minimally compromised by the filtering procedure emerges. In rare cases, the filtered out material distribution can even increase the performance. In addition, we apply hard constraints over the density matrix in a square area enclosing the dipole source. Since uncertainties in the SPS location are expected in the experiment, the close vicinity of the source (a $60 \times 60 \text{ nm}^2$) remains intact throughout the entire optimization process.

To converge to a fully-binarized refractive index distribution, we apply *the binary push* to the material density matrix in the form of a Heaviside filter,^{14,15}

$$\varepsilon_{ij} = \frac{\tanh(\gamma\sigma) + \tanh\left[\gamma(\rho_{ij} - \sigma)\right]}{\tanh(\gamma\sigma) + \tanh\left[\gamma(1 - \sigma)\right]} \quad (\text{S15})$$

where γ and σ are the coefficients determining the strength and direction of the binary push. This step ensures that the design is converged within reasonable amounts of iterations. The optimization stops when the overall binarization of the spatial voxels is above 95%. After this point, un-binarized voxels are forced to take binary values by thresholding.

Changing the SPS position (optional): Localization of SPS in host medium is a challenging task which is often diffraction-limited by optical detection systems.¹⁶ Therefore, the optimization scheme has a robustness implementation in which the SPS

(forward simulation source) is randomly placed in tangential directions with pre-selected limits in length multiple times at each iteration. The number of the forward simulation at each step is dictated by amount point which is required to be scanned. All the forward fields along with their respective FoMs are recorded separately for gradient calculation in the next steps. We note that the step explained here is optional and only necessary for enabling the design robustness.

Computing the FoM, Forward and Adjoint Fields with the FDTD solver: The overall optimization procedure is done using the Matlab scripting language as an application programming interface coupled with a commercial finite-difference time-domain solver (Lumerical FDTD). Fields related to forward/adjoint simulations and FoM are recorded with field monitors at the waveguide cross-section s and optimization domain D . The FoM is computed from equation (S3).

Selecting Fields for the SPS position with the Minimal FoM (optional): To achieve robustness against SPS displacement, TO procedure must ensure that the worst location in terms of FoM within the uncertainty limits yields reasonably well-performing devices. Therefore, maximin decision rule is applied as the forward field selection criterion where the fields of the location with the minimal FoM are selected for gradient calculation.

Calculating the Gradients: Recorded fields in the optimization area from forward/adjoint simulations are 3D data structures. However, we are only interested in multilayer structures with translation symmetry in vertical direction. We average the fields along the vertical z -direction to account for contribution from each layer in D . After collapsing the 3D E -fields into 2D matrix, the gradient is calculated through,

$$\nabla_{\rho} C_{ij} = \sum_{ij} \partial_{\varepsilon_{ij}} C_{ij} \nabla_{\rho} \varepsilon_{ij} \quad (\text{S16})$$

The first multiplicand on the left-hand side is calculated with (S11) while the second one is obtained by applying the chain rule to (S13)-(S15).

Updating the Material Density Distribution: At every iteration, calculated fields inside the 3-D optimization area are collapsed to the 2-D matrix to match matrix ρ by averaging the fields in FDTD mesh grid points in the vertical z -direction. Therefore, material composition is identical in this direction inside the optimization area. Then, these fields are used to calculate gradients ($\nabla_{\rho} C_n$) which are scaled by the selected amount and added to the index density matrix (ρ_n).

$$\rho_{n+1} = \rho_n + \alpha \nabla_{\rho} C_n \quad (\text{S17})$$

Stop Condition (Binarization > 95%): Once ratio of the number of voxels with dielectric constants equal to Air/Si₃N₄ to all voxels reaches a desired threshold (95% for this study), the material density matrix is completely binarized by thresholding all the voxels and forcing them to assume a binary value. This condition greatly helps with time reduction since reaching a fully-binarized distribution without extreme binarization coefficients can take significant number of iterations where the same structure with virtually no changes is calculated repeatably.

S4 Dimensionality Reduction Analysis and Design Rule Derivation

Adjoint TO is gradient-descent based optimization method which converges to the local minima points in the parameter hyperplane. Therefore, initial material density distribution is critical to fully-optimized design performance. For the particular case of this study, an intuitive structure for high coupling efficiency is shown in Fig. S4. A tapered waveguide cross-section ensuring the impedance match between the SPS and the fundamental mode of the waveguide is placed in the area connecting the two and a Bragg-like reflector reflecting and channeling energy into the waveguide is placed at the back of the optimization area. Intuition of similar nature can be obtained through deep exploration of the topologically optimized couplers, which can be used to access even higher-performing devices in shorter design times.

Using the inverse design method outlined above, we produce 2 datasets containing 86 fully optimized devices for two different configurations of the HBN flake. The optimized designs are handled as 201×201-pixel images, whereas their figure of merit (coupling efficiency) becomes their labels. Each device (image) has a different performance (label), so that grouping them directly would not highlight their similarities. Therefore, we quantized the vector of performance labels by k -means clustering.¹⁷ This method partitions arbitrary amounts of observations into the desired number of clusters where each observation belongs to a cluster with the nearest mean. We found out that having 4 centroids for both datasets are sufficient. We followed different approaches for the different datasets. For the “embedded” configuration, we directly applied t-SNE to the dataset with 8 perplexities, a learning rate of 400, and 1000 iterations. For the “on top” configuration, we started with a PCA (Principal Component Analysis) initialization. We took projections of the images on 5-element vectors. Later, we applied t-SNE with 10 perplexities, a learning rate of 200 within 1000 iterations.

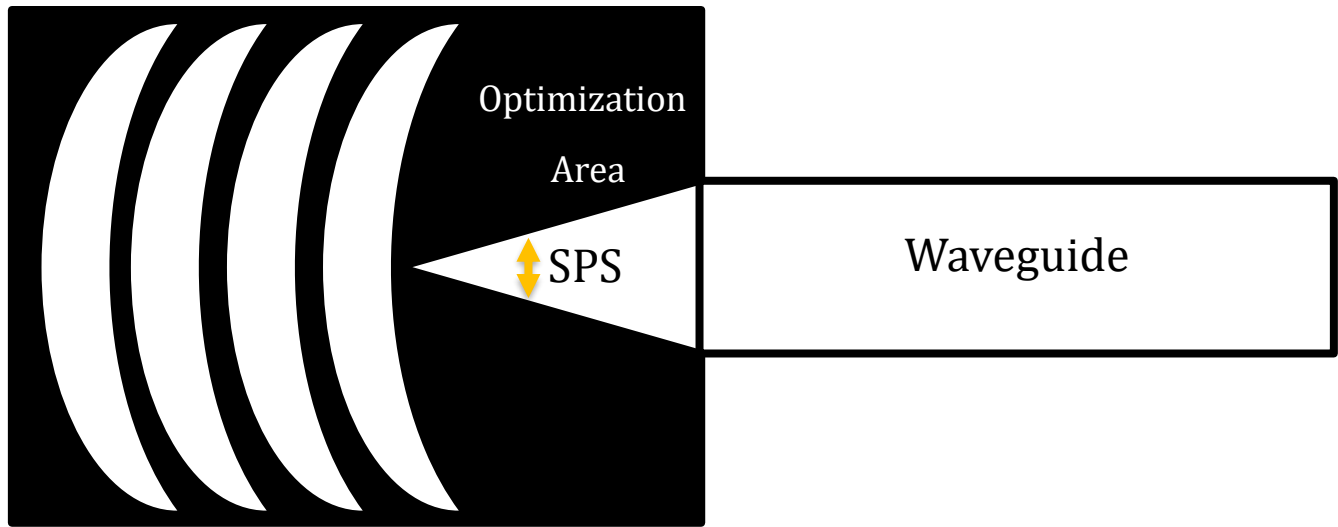


Fig. S 4. Top view artistic rendition of an intuitive human design for the SPS-to-waveguide coupler. Black and white indicate the areas filled with air and Si_3N_4 , respectively.

After creating meaningful t-SNE maps, we performed a manual analysis. In this procedure, we essentially performed simple matrix operations between the images, such as averaging a cluster in a t-SNE plot or locating mutual material/hole features between the samples by intersection. After a comprehensive analysis step, we arrived at the design rules presented in the paper. We created smaller datasets with the derived design rules where all the devices are high performing compared to original datasets. The design rules are applied in the form of (i) enforced material distributions in the selected locations and (ii) intuitive initial material density distributions, shown in Fig. 3 of the main text. The enforced material distribution in certain areas does not change throughout the optimization. These regions are mainly (a) the proximity of the SPS (see the red square in Fig. 3cd of the main text), and (b) the cross-section connecting the SPS and the waveguide (the red segments in Figs. 3cd of the main text).

References

- (1) Boutami, S.; Fan, S. Efficient Pixel-by-Pixel Optimization of Photonic Devices Utilizing the Dyson's Equation in a Green's Function Formalism: Part II Implementation Using Standard Electromagnetic Solvers. *Journal of the Optical Society of America B* **2019**, *36* (9). <https://doi.org/10.1364/JOSAB.36.002387>.
- (2) Lalau-Keraly, C. M.; Bhargava, S.; Miller, O. D.; Yablonovitch, E. Adjoint Shape Optimization Applied to Electromagnetic Design. *Optics Express* **2013**, *21* (18). <https://doi.org/10.1364/OE.21.021693>.
- (3) Deng, Y.; Korvink, J. G. Topology Optimization for Three-Dimensional Electromagnetic Waves Using an Edge Element-Based Finite-Element Method. *Proceedings of the Royal Society A: Mathematical, Physical and Engineering Sciences* **2016**, *472* (2189). <https://doi.org/10.1098/rspa.2015.0835>.
- (4) Jensen, J. S.; Sigmund, O. Topology Optimization for Nano-Photonics. *Laser & Photonics Reviews* **2011**, *5* (2). <https://doi.org/10.1002/lpor.201000014>.
- (5) Bendsoe, M. P.; Sigmund, O. *Topology Optimization*; Springer Berlin Heidelberg: Berlin, Heidelberg, 2004. <https://doi.org/10.1007/978-3-662-05086-6>.
- (6) Hughes, T. W.; Minkov, M.; Williamson, I. A. D.; Fan, S. Adjoint Method and Inverse Design for Nonlinear Nanophotonic Devices. *ACS Photonics* **2018**, *5* (12). <https://doi.org/10.1021/acsphotonics.8b01522>.
- (7) Piggott, A. Y.; Ma, E. Y.; Su, L.; Ahn, G. H.; Sapra, N. v.; Vercruyssen, D.; Netherton, A. M.; Khope, A. S. P.; Bowers, J. E.; Vučković, J. Inverse-Designed Photonics for Semiconductor Foundries. *ACS Photonics* **2020**, *7* (3). <https://doi.org/10.1021/acsphotonics.9b01540>.
- (8) Dietrich Marcuse. *Theory of Dielectric Optical Waveguides*, 2nd ed.; Academic: Boston, 1991; Vol. Chapter 3.
- (9) Jackson, J. D. Electrodynamics, Classical. In *digital Encyclopedia of Applied Physics*; Wiley-VCH Verlag GmbH & Co. KGaA: Weinheim, Germany, 2003. <https://doi.org/10.1002/3527600434.eap109>.
- (10) Michaels, A.; Yablonovitch, E. Leveraging Continuous Material Averaging for Inverse Electromagnetic Design. *Optics Express* **2018**, *26* (24). <https://doi.org/10.1364/OE.26.031717>.
- (11) Iguchi, A.; Tsuji, Y.; Yasui, T.; Hirayama, K. Efficient Topology Optimization of Optical Waveguide Devices Utilizing Semi-Vectorial Finite-Difference Beam Propagation Method. *Optics Express* **2017**, *25* (23). <https://doi.org/10.1364/OE.25.028210>.

- (12) Su, L.; Vercruysse, D.; Skarda, J.; Sapra, N. v.; Petykiewicz, J. A.; Vučković, J. Nanophotonic Inverse Design with SPINS: Software Architecture and Practical Considerations. *Applied Physics Reviews* **2020**, *7* (1). <https://doi.org/10.1063/1.5131263>.
- (13) Christiansen, R. E.; Sigmund, O. Inverse Design in Photonics by Topology Optimization: Tutorial. *Journal of the Optical Society of America B* **2021**, *38* (2). <https://doi.org/10.1364/JOSAB.406048>.
- (14) Guest, J. K. Topology Optimization with Multiple Phase Projection. *Computer Methods in Applied Mechanics and Engineering* **2009**, *199* (1–4), 123–135. <https://doi.org/10.1016/j.cma.2009.09.023>.
- (15) Sigmund, O. Morphology-Based Black and White Filters for Topology Optimization. *Structural and Multidisciplinary Optimization* **2007**, *33* (4–5), 401–424. <https://doi.org/10.1007/s00158-006-0087-x>.
- (16) Feng, J.; Deschout, H.; Caneva, S.; Hofmann, S.; Lončarić, I.; Lazić, P.; Radenovic, A. Imaging of Optically Active Defects with Nanometer Resolution. *Nano Letters* **2018**, *18* (3). <https://doi.org/10.1021/acs.nanolett.7b04819>.
- (17) MacQueen, J. Some Methods for Classification and Analysis of Multivariate Observations. In *Proceedings of the fifth Berkeley Symposium on Mathematical Statistics and Probability*; 1967; Vol. 1.